Analytical solution for dynamic evaporation of liquid in isothermal condition

Luiz Eduardo Czelusniak,[1,2,*] Tim Niklas Bingert,[1,3] Stephan Simonis,[1,2]
Alexander J. Wagner,[4] and Mathias J. Krause[1,2,3]

[1]*Lattice Boltzmann Research Group (LBRG), Karlsruhe Institute of Technology (KIT), 76131 Karlsruhe, Germany*
[2]*Institute for Applied and Numerical Mathematics (IANM), Karlsruhe Institute of Technology (KIT), 76131 Karlsruhe, Germany*
[3]*Institute of Mechanical Process Engineering (MVM), Karlsruhe Institute of Technology (KIT), 76131 Karlsruhe, Germany*
[4]*Department of Physics, North Dakota State University (NDSU), Fargo, North Dakota 58102, USA*

(Received 4 June 2025; revised 15 January 2026; accepted 24 February 2026; published 10 April 2026)

An analytical solution based on a diffuse-interface model is presented for an isothermal evaporation problem at subsaturated vapor pressure. The macroscopic equations are derived from the free-energy formulation widely used in the lattice Boltzmann literature, distinguishing our approach from conventional evaporation models that rely on jump conditions or purely kinetic theory. The interface behavior is fully described by differential equations, eliminating the need for assumptions such as local thermodynamic equilibrium at the interface. We derive an exact analytical solution for the inviscid case and propose an approximate solution that accounts for viscous effects. Our model reveals a relationship between evaporation rate and viscosity within the diffuse-interface framework. The analytical results are validated against numerical simulations using the open-source parallel library openlb, demonstrating excellent agreement within the framework of diffuse-interface methods.

DOI: 10.1103/4dl9-1x8s

I. INTRODUCTION

Understanding and predicting the evaporation phenomena is crucial for engineering applications, e.g., food drying [1], industrial dehydration [2], distillation process [3], vacuum evaporation [4], paint drying [5], evaporative cooling [6], steam power generation [7], and others. There are different ways to study this phenomenon: analytically [8–16], numerically [17–19], and experimentally [20–22]. For highly complex problems, numerical and experimental approaches are essential. However, the analytical method provides physical insights that lead to a deeper understanding of the phenomenon, making it highly valuable.

There is extensive literature on evaporation modeling. An important result is the Hertz-Knudsen relation [8–11]. Another significant contribution involving kinetic theory was made by Schrage [12], who calculated evaporation fluxes of pure substances and multicomponent systems. Notable results employing macroscopic phase change modeling include the one-dimensional Stefan problem [13], originally developed for a solid-liquid phase transition and Scriven's solution [14] for droplet evaporation. Recent articles extend these approaches to more complex situations [15,16].

Another approach to modeling multiphase systems that has gained popularity in numerical studies is the diffuse-interface model. This model treats the interface as a thin region in which fluid properties continuously transition between the vapor and liquid phases. The phase-field model [23–25], which usually employs the Cahn-Hilliard [26,27] or the Allen-Cahn [28] equation, is a diffuse-interface model used in combination with several numerical methods, for example, lattice Boltzmann methods (LBMs) [29], finite-element methods (FEMs) [30], and finite volume (FV) [31] or immersed boundary methods (IBMs) [32]. Other examples of diffuse-interface model-based methods are the free-energy [33–35] and the pseudopotential [36,37] LBMs, which are single-component methods capable of modeling a liquid-vapor phase transition without any special treatment of the interface. Due to good parallelizability and robustness, LBM is generally well suited for complex flow applications [38–41], even at large scales [42]. Notably, many of the diffuse-interface models listed above (or derivates thereof) are implemented in open-source libraries such as openlb [43] and thus readily available for parallel execution on personal devices or clusters of any size.

While diffuse-interface models such as Cahn-Hilliard are well established in numerical and analytical studies of phase separation [44], their use in analytical descriptions of liquid evaporation processes remains limited. However, these models also hold great potential for the development of analytical solutions since the fluid behavior is fully described by differential equations. This eliminates the need for assumptions such as local equilibrium at the interface, which is commonly used in sharp-interface modeling. This represents a significant advancement in the analysis of nonequilibrium thermodynamics.

In this work, we employ a diffuse-interface model to study the evaporation process. To simplify the problem, we consider an isothermal system subject to a subsaturation pressure condition. A similar system was previously studied by Jamet [45], but using a sharp-interface approach. With our

*Contact author: luiz.czelusniak@partner.kit.edu

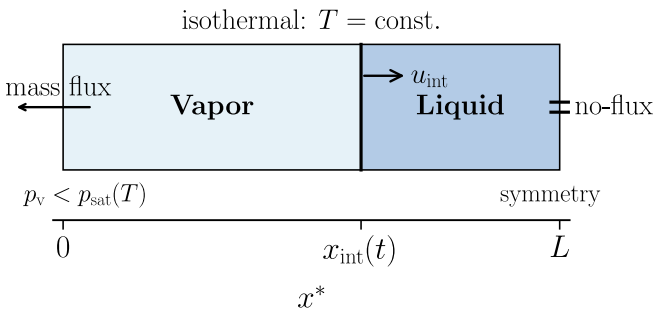

FIG. 1. Schematic representation of the one-dimensional isothermal evaporation problem under subsaturated vapor pressure. The system consists of a vapor region on the left and a liquid region on the right, separated by a flat interface located at $x_{\text{int}}(t)$. A pressure $p_v < p_{\text{sat}}(T)$ is imposed at the vapor boundary, which drives evaporation and causes the interface to move toward the liquid phase with velocity u_{int}. The right boundary represents a plane of symmetry, where $u = 0$ and $\partial_x \rho = 0$.

innovative methodology, we observed a dependence of the evaporation rate on the fluid viscosity—a behavior that has not been captured by any existing model in the literature. Finally, we derived an analytical solution for the evaporation rate in the inviscid case and an approximate solution for the viscous case. The predictions from our solutions are confirmed by simulations using an LBM implemented in the open-source parallel library openlb [43].

The practical applications of our analytical solution are as follows: First, it provides predictions that can be tested in experiments to validate diffuse-interface methods or suggest future corrections to this approach. Second, our solution can also be used to construct benchmark cases to test numerical approaches for diffuse-interface models. Third, predicting evaporation phenomena under subsaturation pressure is crucial in, e.g., fuel injection systems, especially within low-pressure chambers. This process has significant implications for combustion engines [46]. In future works, our approach of constructing an analytical solution can be extended to nonisothermal and multicomponent problems.

The article is organized as follows: In Sec. II, the physical problem of isothermal evaporation under subsaturation pressure is introduced. In Sec. III, the governing equations are presented. Section IV details the analytical solution procedure, including the derivation of the interface velocity and its dependence on physical parameters. In Sec. VI, the analytical solution is evidenced through comparisons with LBM simulations, and the influence of viscosity and pressure differences on the interface dynamics is analyzed. Finally, in Sec. VII, we summarize and discuss the main findings and propose directions for future work.

II. PROBLEM DESCRIPTION

The problem considered in this work is a dynamic, isothermal liquid-vapor evaporation process, similar to that described by Jamet [45]. We consider a system consisting of two phases, liquid and vapor, separated by a flat interface. Owing to this geometry, the problem reduces to a one-dimensional configuration, as illustrated in Fig. 1. The temperature T is uniform

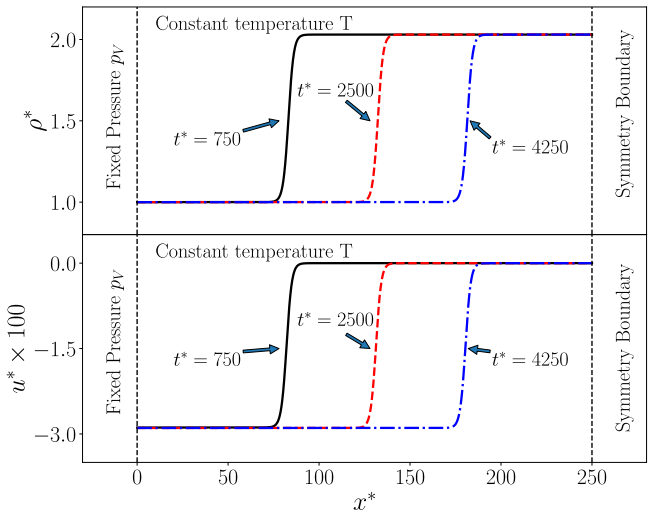

FIG. 2. Top: Density profile ρ^* as a function of domain coordinate x^* at three instants t^*. Bottom: Velocity profile u^* for the same conditions. All quantities are dimensionless and defined in (5). Simulations conducted with the model of Wagner [47] implemented in openlb [43] (see Sec. V for details).

and constant throughout the domain. At equilibrium, the system exhibits a homogeneous pressure equal to the saturation pressure $p_{\text{sat}}(T)$. We investigate the system behavior when a subsaturated pressure $p_v < p_{\text{sat}}(T)$ is imposed in the vapor phase, which induces steady evaporation of the liquid region.

To illustrate this phenomenon, we perform a numerical simulation using the free-energy LBM formulation proposed by Wagner [47]. Figure 2 shows the density and velocity fields obtained from the numerical simulation. The top panel shows the density profile ρ^* at three time instants ($t^* = 750$, $t^* = 2500$, and $t^* = 4250$). On the left boundary (vapor phase), a pressure lower than the saturation pressure, $p_v = 0.99 p_{\text{sat}}$, is imposed. The superscript $*$ indicates dimensionless quantities such as t^*. The definition of the dimensionless quantities is presented in Sec. III. The simulation details are presented in Sec. V.

The density profile in Fig. 2 exhibits three distinct regions, which are typical of diffuse-interface models. On the far left, the density is uniform and equal to the vapor bulk value ρ_v, whereas on the far right, it is uniform and equal to the liquid bulk value ρ_l. Between these two constant-density regions lies a thin transition layer where the density varies smoothly from ρ_v to ρ_l, representing the diffuse interface. From $t^* = 750$ to $t^* = 4250$, this liquid region becomes progressively smaller, demonstrating that the imposed boundary condition leads to a sustained evaporation process. The lower panel of Fig. 2 shows the corresponding velocity profile. In the liquid region, the velocity remains zero due to symmetry, whereas in the vapor region, the velocity profile confirms that mass exits the domain through the left boundary.

This simulation was performed for a uniform dimensionless viscosity $\nu^* = 1$. We repeated the simulation for different viscosity values and recorded the interface position for several other time instants. For consistency, the interface location was extracted as the point where the density reaches the midpoint between the bulk phases, $\rho = \frac{1}{2}(\rho_v + \rho_l)$. The results are

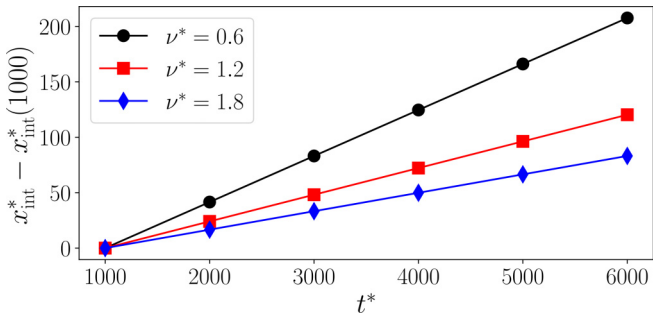

FIG. 3. Interface displacement, $x^*_{\rm int}(t^*) - x^*_{\rm int}(t^* = 1000)$, as a function of time t^* for several viscosities ν^*. All quantities are dimensionless and defined in (5). Simulations were performed using the model of Wagner [47] implemented in openlb [43] (see Sec. V for details). The interface position is defined, in the context of a diffuse-interface method, as the location where the fluid density reaches the midpoint value, $\rho = \frac{1}{2}(\rho_{\rm v} + \rho_{\rm l})$, where $\rho_{\rm v}$ and $\rho_{\rm l}$ are the vapor and liquid densities, respectively.

summarized in Fig. 3. Two interesting behaviors are observed. First, for sufficiently long simulation times, the "position vs time" curve is a straight line, which implies a constant interface velocity. The second surprising result is that the interface velocity depends on the fluid viscosity. This dependence of the evaporation rate on fluid viscosity is not present in classical evaporation models [8,9,12] or in analytical solutions to evaporation problems [13,14], showing a different behavior.

In the next sections, we focus on obtaining an analytical solution that describes this physical phenomenon.

III. GOVERNING EQUATIONS

This problem is modeled by the one-dimensional (1D) mass and momentum conservation equations,

$$\frac{\partial \rho}{\partial t} + \frac{\partial (\rho u)}{\partial x} = 0, \tag{1a}$$

$$\rho \frac{\partial u}{\partial t} + \rho u \frac{\partial u}{\partial x} = -\frac{\partial p}{\partial x} + \frac{\partial \tau_{xx}}{\partial x}, \tag{1b}$$

where ρ denotes the density, u is the velocity, p is the pressure, and τ_{xx} is the viscous stress as presented in Krüger *et al.* [48, p. 6]:

$$\tau_{xx} = \left(\frac{4}{3}\nu + \nu_{\rm b}\right)\rho \frac{\partial u}{\partial x}, \tag{2}$$

and, unless stated otherwise, all variables depend on time t and space x. The symbols $\nu > 0$ and $\nu_{\rm b}$ in (2) represent the shear and bulk kinematic viscosity coefficients, respectively. For dilute monatomic gases, kinetic theory [49] predicts $\nu_{\rm b} = 0$, which coincides with Stokes' hypothesis [50]. Notably, the bulk viscosity for nonideal fluids is a complex topic [51,52]. In addition, the stress-tensor behavior at the interface is barely described in the literature.

In particular, in this work, we compare the analytical solution of a problem governed by Eqs. (1a) and (1b) with the numerical simulations performed with LBM based on an isothermal flow assumption. Thus, we use a different stress-tensor definition than (2), i.e.,

$$\tau_{xx} = 2\nu\rho \frac{\partial u}{\partial x}. \tag{3}$$

The alternative form of the stress tensor given in (3), compared to the complete expression in (2), arises from the fact that the bulk viscosity predicted by the Bhatnagar-Gross-Krook [53]-based lattice Boltzmann model is incompatible with the assumption of isothermal flow. Unless stated otherwise, we continue with the stress tensor defined in (3). The implications of this consideration can be tested and, if necessary, future corrections can be made.

In addition, we use a Korteweg-type pressure [54]

$$p = p_{\rm EOS} + \frac{\kappa}{2}\left(\frac{\partial \rho}{\partial x}\right)^2 - \kappa\rho \frac{\partial^2 \rho}{\partial x^2}, \tag{4}$$

where $p_{\rm EOS}$ denotes the equation of state (EOS) and $\kappa > 0$ is the surface tension coefficient.

A fixed pressure $p_{\rm v}$ is imposed on the boundary. Since the temperature is fixed, this will imply a fixed vapor density at the boundary $\rho_{\rm v}$. Then, we define the following dimensionless quantities:

$$x^* := \frac{x}{\rho_{\rm v}}\sqrt{\frac{p_{\rm v}}{\kappa}}, \quad t^* := t\frac{p_{\rm v}}{\sqrt{\rho_{\rm v}^3 \kappa}}, \quad u^* := u\sqrt{\frac{\rho_{\rm v}}{p_{\rm v}}},$$
$$\nu^* := \frac{\nu}{\sqrt{\rho_{\rm v}\kappa}}, \quad \rho^* := \frac{\rho}{\rho_{\rm v}}, \quad p^* := \frac{p}{p_{\rm v}}. \tag{5}$$

Equation (5) defines the set of dimensionless quantities employed in this work, including the dimensionless viscosity $\nu^* := \nu/\sqrt{\rho_{\rm v}\kappa}$.

IV. ANSATZ FOR A MODEL SOLUTION

When performing initial simulations, we observed that the interface was moving with a constant speed (cf. Fig. 3). Thus, in the ansatz used further below to derive an analytical solution, we make explicit use of the following assumptions:

(1) After a transient time, the solution reaches a state where the interface propagates with constant velocity $u_{\rm int}$.

(2) The right boundary will have a zero velocity by symmetry and will retain a constant density.

(3) The previous assumptions suggest that we can pick a reference frame (x', t') that moves with the interface, where any field ϕ is then independent of time, i.e., $\partial\phi/\partial t' = 0$.

The transformation between the old and new frames of reference is

$$x' = x - u_{\rm int}t,$$
$$t' = t, \quad x = x' + u_{\rm int}t',$$
$$t = t'. \tag{6}$$

From the definitions in (6) and the consideration of Assumption 3 above, it follows that

$$\frac{\partial \phi}{\partial t} = \left(\frac{\partial \phi}{\partial t'}\right)\frac{\partial t'}{\partial t} + \left(\frac{\partial \phi}{\partial x'}\right)\frac{\partial x'}{\partial t} \Rightarrow \frac{\partial \phi}{\partial t} = -u_{\rm int}\frac{\partial \phi}{\partial x'},$$
$$\frac{\partial \phi}{\partial x} = \left(\frac{\partial \phi}{\partial t'}\right)\frac{\partial t'}{\partial x} + \left(\frac{\partial \phi}{\partial x'}\right)\frac{\partial x'}{\partial x} \Rightarrow \frac{\partial \phi}{\partial x} = \frac{\partial \phi}{\partial x'}. \tag{7}$$

A. Mass conservation

Now, the mass conservation equation (1a) is rewritten in terms of x'. Since the solution is independent of t', we write $\partial\phi/\partial x' = d\phi/dx'$, which gives

$$-u_{\text{int}}\frac{d\rho}{dx'} + \frac{d(\rho u)}{dx'} = 0 \Rightarrow (u_{\text{int}} - u)\frac{d\rho}{dx'} = \rho\frac{du}{dx'}. \tag{8}$$

We integrate (8) and obtain a relation between ρ and u up to a constant C_1,

$$\int \frac{d\rho}{\rho} = \int \frac{du}{u_{\text{int}} - u} + C_1 \Rightarrow \rho(u_{\text{int}} - u) = \mathrm{e}^{C_1} = \text{const.} \tag{9}$$

According to Assumpion 2, in the liquid region, $\rho = \rho_{\text{l}}$ and $u = 0$, respectively. Then, from (9), we obtain

$$\rho(u_{\text{int}} - u) = \rho_{\text{l}} u_{\text{int}}. \tag{10}$$

Thus, our main finding from the mass conservation equation (1a) is (10), which leads to the useful relation

$$\frac{du}{dx'} = \frac{(u_{\text{int}} - u)}{\rho}\frac{d\rho}{dx'} \Rightarrow \frac{du}{dx'} = \frac{\rho_{\text{l}} u_{\text{int}}}{\rho^2}\frac{d\rho}{dx'}. \tag{11}$$

We make explicit use of (11) below.

B. Momentum conservation

Considering the momentum equation (1b), we start by replacing the derivatives in terms of t and x with derivatives in terms of x', which gives

$$-\rho u_{\text{int}}\frac{du}{dx'} + \rho u\frac{du}{dx'} = -\frac{dp}{dx'} + \frac{d}{dx'}\left(2\nu\rho\frac{du}{dx'}\right). \tag{12}$$

Next, we rewrite the left-hand side of (12) using (10) and (11) to obtain

$$\rho(u - u_{\text{int}})\frac{du}{dx'} = -\frac{\rho_{\text{l}}^2 u_{\text{int}}^2}{\rho^2}\frac{d\rho}{dx'}. \tag{13}$$

Using (11), we also rewrite the viscous term as

$$2\nu\rho\frac{du}{dx'} = 2\rho_{\text{l}} u_{\text{int}}\frac{\nu}{\rho}\frac{d\rho}{dx'}. \tag{14}$$

Now, all terms of (12) that were dependent on u are replaced by terms that depend on ρ. Hence, we have reached a closed-form equation that depends on one variable only. All terms of the modified momentum conservation equation based on (12)–(14) can be grouped in the form

$$\frac{d}{dx'}\left(p + \frac{(\rho_{\text{l}} u_{\text{int}})^2}{\rho} - 2\rho_{\text{l}} u_{\text{int}}\frac{\nu}{\rho}\frac{d\rho}{dx'}\right) = 0, \tag{15}$$

which gives

$$p + \frac{(\rho_{\text{l}} u_{\text{int}})^2}{\rho} - 2\rho_{\text{l}} u_{\text{int}}\frac{\nu}{\rho}\frac{d\rho}{dx'} = C_2 = \text{const.} \tag{16}$$

Considering that density gradients are equal to zero in the bulk regions, we can evaluate the constant C_2 in (16) and obtain

$$C_2 = p_{\text{v}} + \frac{\rho_{\text{l}}^2 u_{\text{int}}^2}{\rho_{\text{v}}} \quad \text{and} \quad C_2 = p_{\text{l}} + \frac{\rho_{\text{l}}^2 u_{\text{int}}^2}{\rho_{\text{l}}}. \tag{17}$$

Next, we proceed by manipulating the differential equation in a more convenient form to solve.

C. Final ordinary differential equation

From (4), (16), and (17), we have the following ordinary differential equation (ODE) in terms of x':

$$\kappa\rho\frac{d^2\rho}{dx'^2} - \frac{\kappa}{2}\left(\frac{d\rho}{dx'}\right)^2 + 2\rho_{\text{l}} u_{\text{int}}\frac{\nu}{\rho}\frac{d\rho}{dx'} = f(\rho), \tag{18a}$$

where

$$f(\rho) = p_{\text{EOS}} - p_{\text{v}} - u_{\text{int}}^2\rho_{\text{l}}^2\left(\frac{1}{\rho_{\text{v}}} - \frac{1}{\rho}\right). \tag{18b}$$

The ODE (18a) can be converted into a more convenient form by applying a simplification based on the assumption that the density function $\rho = \rho(x')$ is monotonically growing, i.e., $d\rho/dx' > 0$ for all x'. Then, the dependency on x' can be transformed into a dependency on ρ.

Considering $d\rho/dx'$ as a function of ρ, we have that

$$\begin{aligned}
&\frac{d\rho}{dx'} = z(\rho),\\
&\frac{d^2\rho}{dx'^2} = \frac{dz}{dx'} \Rightarrow \frac{d^2\rho}{dx'^2} = \frac{dz}{d\rho}\frac{d\rho}{dx'} \Rightarrow \frac{d^2\rho}{dx'^2} = \frac{1}{2}\frac{dz^2}{d\rho}.
\end{aligned} \tag{19}$$

Also, the first two terms of the left-hand side of (18a) can be grouped such that

$$\begin{aligned}
&\kappa\rho\frac{d^2\rho}{dx'^2} - \frac{\kappa}{2}\left(\frac{d\rho}{dx'}\right)^2 = \frac{\kappa\rho}{2}\frac{dz^2}{d\rho} - \frac{\kappa}{2}z^2\\
&\Rightarrow \kappa\rho\frac{d^2\rho}{dx'^2} - \frac{\kappa}{2}\left(\frac{d\rho}{dx'}\right)^2 = \frac{\rho^2}{2}\frac{d}{d\rho}\frac{z^2}{\rho}.
\end{aligned} \tag{20}$$

By applying the transformations of (20) to (18a), we obtain a nonlinear ODE,

$$\frac{d}{d\rho}\frac{z^2}{\rho} + 4\frac{\rho_{\text{l}} u_{\text{int}}}{\kappa}\frac{\nu}{\rho^3}z = \frac{2}{\kappa}\frac{f(\rho)}{\rho^2}. \tag{21}$$

The ODE (21) is an Abel's equation of the second kind. This equation has the general form [55]

$$[g_0(\rho) + g_1(\rho)z]\frac{dz}{d\rho} = f_2(\rho)z^2 + f_1(\rho)z + f_0(\rho). \tag{22}$$

Equation (21) is a particular case of (22) with coefficients,

$$\begin{aligned}
&g_0(\rho) = 0, \quad g_1(\rho) = \frac{2}{\rho},\\
&f_0(\rho) = \frac{2}{\kappa}\frac{f(\rho)}{\rho^2}, \quad f_1(\rho) = -4\frac{\rho_{\text{l}} u_{\text{int}}}{\kappa}\frac{\nu}{\rho^3},\\
&f_2(\rho) = \frac{1}{\rho^2}.
\end{aligned} \tag{23}$$

Looking for a general solution to (21) may not be worth the effort, as the procedure could be too complex for practical applications. Therefore, we will proceed with an approximate solution.

D. Exact solution of inviscid case

The simplest case occurs when there is no viscosity, $\nu = 0$. Thus, (21) can be simplified,

$$\frac{d}{d\rho}\frac{z^2}{\rho} = \frac{2}{\kappa}\frac{f(\rho)}{\rho^2}. \tag{24}$$

Next, we integrate the whole expression

$$\frac{z^2(\rho)}{\rho} - \frac{z_v^2}{\rho_v} = \int_{\rho_v}^{\rho} \frac{2}{\kappa}\frac{f(\rho)}{\rho^2} d\rho, \tag{25}$$

where $z_v = z(\rho_v)$. The boundary condition $z_v = 0$ (no density gradients in the bulk phases) is applied to obtain a solution for $z(\rho)$,

$$z^{(0)}(\rho) = \sqrt{\rho \int_{\rho_v}^{\rho} \frac{2}{\kappa}\frac{f(\rho)}{\rho^2} d\rho}. \tag{26}$$

The symbol $z^{(0)}$ represents the solution of z for the inviscid case. The selection of the positive sign in the solution (26) means that the interface density grows with respect to the x direction. In Fig. 2, this represents the interface in the left-hand side.

Then, we replace $f(\rho)$ in (26) by (18b), and apply the boundary conditions $z_L = z(\rho_L) = 0$ (no density gradients in the bulk phases). After this step, we obtain the following expression:

$$0 = \int_{\rho_v}^{\rho_l} \frac{p_{EOS} - p_v}{\rho^2} d\rho - \int_{\rho_v}^{\rho_l} \frac{u_{int}^2 \rho_l^2}{\rho^2}\left(\frac{1}{\rho_v} - \frac{1}{\rho}\right) d\rho. \tag{27}$$

Finally, we perform the integral in the second term of the right-hand side of (27) and isolate u_{int},

$$u_{int}^{(0)} = \frac{\sqrt{\int_{\rho_v}^{\rho_l} \frac{p_{EOS} - p_v}{\rho^2} d\rho}}{\sqrt{\frac{\rho_l}{\rho_v}\left(\frac{1}{2}\frac{\rho_l}{\rho_v} - 1\right) + \frac{1}{2}}}, \tag{28}$$

where $u_{int}^{(0)}$ represents the interface velocity for the inviscid case. The positive velocity is compatible with the orientation of the interface (26) (see Fig. 2). The inviscid interface velocity is completely independent of κ. An important consideration regarding (28) is the dependence of the liquid density ρ_l on the interface velocity. As a result, determining the correct liquid velocity requires solving a coupled system comprising (28) and the following two additional equations:

$$p_l = p_v + \rho_l^2 u_{int}^2 \left(\frac{1}{\rho_v} - \frac{1}{\rho_l}\right), \quad p_l = p_{EOS}(\rho_l, T). \tag{29}$$

Next, we consider the case with viscous effects.

E. Approximate solution of viscid case

The equivalent of (25) for the viscid case is

$$\frac{z^2(\rho)}{\rho} - \frac{z_v^2}{\rho_v} = \int_{\rho_v}^{\rho} \left[\frac{2}{\kappa}\frac{f(\rho)}{\rho^2} - 4\frac{\rho_l u_{int}}{\kappa}\frac{\nu}{\rho^3} z(\rho)\right] d\rho. \tag{30}$$

The problem with (30) is that we cannot use it to explicitly solve for z. To overcome this challenge and obtain an approximate solution, we consider that the viscosity ν has a small influence on the interface profile, which depends on z. At least, this approximation will be valid for sufficiently small ν. Thus, we assume that z in the viscous case can be approximated by $z^{(0)}$ from the inviscid case. We use this approximation to compute the integral of the second term on the right-hand side of (30).

Applying the boundary condition $z_l = 0$ and the previous assumption to (30) yields

$$0 = \int_{\rho_v}^{\rho_l} \left[\frac{2}{\kappa}\frac{f(\rho)}{\rho^2} - 4\frac{\rho_l u_{int}}{\kappa}\frac{\nu}{\rho^3} z^{(0)}(\rho)\right] d\rho. \tag{31}$$

Replacing $f(\rho)$ in (26) by (18b) leads to a final equation that describes the interface velocity:

$$A u_{int}^2 + B u_{int} + C = 0, \tag{32a}$$

$$A = \frac{\rho_l}{\rho_v}\left(1 - \frac{1}{2}\frac{\rho_l}{\rho_v}\right) - \frac{1}{2}, \tag{32b}$$

$$B = -2\rho_l \int_{\rho_v}^{\rho_l} \frac{\nu}{\rho^3} z^{(0)} d\rho, \tag{32c}$$

$$C = \int_{\rho_v}^{\rho_l} \frac{p_{EOS} - p_v}{\rho^2} d\rho. \tag{32d}$$

Notably, the solution approach above is valid even if ν depends on ρ. The interface velocity is obtained by simply solving the quadratic equation (32a) toward

$$u_{int} = \frac{-B - \sqrt{B^2 - 4AC}}{2A}, \tag{33}$$

where the choice of sign in (33) is motivated by the following reasons:

(i) A is always negative ($A < 0$) if $\rho_v < \rho_l$,
(ii) B is always negative ($B < 0$) if $\rho_v < \rho_l$,
(iii) C is always positive ($C > 0$) for $p_v < p_{sat}(T)$.

Consequently, we conclude that a positive solution for u_{int} is only possible for (33). The positive solution was selected due to the interface orientation choice in (26). The interface velocity must be solved together with the liquid density by coupling (33) with (29). The validity of the solution (33) is examined in Sec. VI.

Although the present derivation is restricted to a planar one-dimensional configuration, the same diffuse-interface formulation can, in principle, be extended to higher-dimensional problems. For geometries with strong symmetry—such as an evaporating cylinder (axisymmetric) or a spherical droplet—the governing equations can be reduced to a one-dimensional form in the radial coordinate, where curvature effects appear through the capillary term in the pressure tensor. This leads to a more general differential equation that could serve as a basis for analytical or approximate solutions in future studies.

V. LATTICE BOLTZMANN METHOD AND openlb IMPLEMENTATION

In this work, we compare the analytical results given by (28) and (32a) against LBM simulations performed using openlb [43]. This is a powerful open-source LBM library applied in various fluid dynamics applications, including subgrid particulate flows [56], fully resolved particle flows [57,58], turbulence simulations [59,60], optimization [61,62], subgrid multiphase flows [39], and fully resolved multiphase flows [35]. The numerical framework employed in this work is based on openlb release 1.8 [63]. A preliminary version of the proposed method is already included in this release, whereas the full implementation of the model will be made publicly available in a future openlb release.

The governing equation is the lattice Boltzmann equation [48], with single-relaxation-time collision operator

$$f_i(t+\Delta t, \boldsymbol{x}+\boldsymbol{c}_i\Delta t) - f_i(t,\boldsymbol{x}) = \frac{\Delta t}{\tau}\left(f_i^{\mathrm{eq}} - f_i\right) + \Delta t F_i, \tag{34}$$

where f_i and f_i^{eq} denote the distribution function and its equilibrium counterpart, respectively. The indexes i label the lattice velocity $\boldsymbol{c}_i$ at which f_i is evaluated. The relaxation time τ is related to the fluid kinematic viscosity $\nu = c_s^2(\tau - 0.5\Delta t)$. The parameter $c_s^2 = (1/3)(\Delta x/\Delta t)^2$ is called lattice sound speed [48]. The equilibrium distribution function depends on the fluid density ρ and the equilibrium velocity u_α^{eq} [64],

$$f_i^{\mathrm{eq}} = w_i\rho\left(1 + \frac{c_{i\alpha}}{c_s^2}u_\alpha^{\mathrm{eq}} + \frac{c_{i\alpha}c_{i\beta} - c_s^2\delta_{\alpha\beta}}{2c_s^4}u_\alpha^{\mathrm{eq}}u_\beta^{\mathrm{eq}}\right), \tag{35}$$

where w_i are the lattice weights for each lattice direction i. The equilibrium velocity is a quantity used to define f_i^{eq} and its relation with the real fluid velocity is introduced later.

The term F_i is called the forcing scheme and accounts for the addition of an external force F_α to the LBM. Wagner [47] proposed the following forcing scheme for the free-energy LBM:

$$F_i = w_i\left[\frac{c_{i\alpha}}{c_s^2}F_\alpha + \frac{c_{i\alpha}c_{i\beta} - c_s^2\delta_{\alpha\beta}}{2c_s^4}\left(F_\alpha u_\beta^{\mathrm{eq}} + F_\beta u_\alpha^{\mathrm{eq}} + \psi\delta_{\alpha\beta}\right)\right]. \tag{36}$$

The external force is given by

$$F_\alpha = -\rho\partial_\alpha\mu + c_s^2\partial_\alpha\rho. \tag{37}$$

The first term on the right-hand side is the thermodynamic force and is related to the gradient of the chemical potential. The second term is a correction since the LBM naturally yields the pressure tensor of an isothermal ideal gas, $p_{\alpha\beta} = \rho c_s^2$, which must be removed. The spatial derivatives are computed using second-order central finite difference stencils.

The cancellation of the original pressure tensor $p_{\alpha\beta} = \rho c_s^2$ is not perfect in the numerical sense. As a result, this leads to numerical errors related to gradients of the density. To this end, a correction term ψ is added to the method,

$$\tau\psi = \left(\tau - \frac{1}{4}\right)\frac{F_\alpha F_\alpha}{\rho} + \frac{1 - C_\psi}{12}\nabla^2\rho. \tag{38}$$

The correction term in (38) was originally designed by Wagner [47] to eliminate higher-order discretization errors and thereby improve the accuracy of the method. In principle, setting $C_\psi = 0$ removes the entire residual of the underlying pressure tensor, yielding the cleanest representation of the continuum limit. However, we found that this complete cancellation also removes a source of artificial numerical diffusion that plays a stabilizing role in practical simulations.

To preserve stability while still keeping the correction effective, we keep a small value for C_ψ in this work. Since this term acts only on discretization errors, its influence vanishes under grid refinement. Accordingly, we carried out a grid-refinement study to ensure that our results are independent of the mesh resolution. For completeness, a direct comparison between the original choice $C_\psi = 0$ and the stabilized value adopted here is presented in Sec. VI, highlighting the regimes in which the proposed strategy significantly enhances numerical stability.

The Wagner forcing has been validated primarily for 1D cases. This means that an extension for 2D cases was not provided yet. The velocity set corresponds to the standard two-dimensional nine-velocity scheme (D2Q9),

$$\boldsymbol{c}_i = \begin{cases} (0,0), & i = 0, \\ (c,0),(0,c),(-c,0),(0,-c), & i = 1,\ldots,4, \\ (c,c),(-c,c),(-c,-c),(c,-c), & i = 5,\ldots,8. \end{cases} \tag{39}$$

The macroscopic variables are computed from the moments of the distribution function,

$$\rho = \sum_i f_i, \tag{40a}$$

$$\rho u_\alpha^{\mathrm{eq}} = \sum_i f_i c_{i\alpha}. \tag{40b}$$

The physical fluid velocity u_α depends on u_α^{eq} and the force F_α,

$$u_\alpha = u_\alpha^{\mathrm{eq}} + \frac{\Delta t}{2}\frac{F_\alpha}{\rho}. \tag{41}$$

In this work, we use an equation of state based on the Landau free-energy functional [65],

$$p_{\mathrm{EOS}} = p_c(\nu_\rho + 1)^2\left(3\nu_\rho^2 - 2\nu_\rho + 1 - 2\tau_w\right), \tag{42a}$$

$$\nu_\rho = \frac{\rho - \rho_c}{\rho_c}, \quad \tau_w = \frac{T_c - T}{T_c}, \tag{42b}$$

where ρ_c, p_c, and T_c are the critical density, pressure, and temperature. The chemical potential is described by

$$\mu = \frac{4p_c}{\rho_c}\nu_\rho\left(\nu_\rho^2 - \tau_w\right) - \kappa\nabla^2\rho. \tag{43}$$

For a planar interface in equilibrium, the bulk densities ($\rho_{\mathrm{v}}^{\mathrm{sat}}$ and $\rho_{\mathrm{l}}^{\mathrm{sat}}$), the parameter ξ (related to the interface thickness), and surface tension γ are given by

$$\rho_{\mathrm{v}}^{\mathrm{sat}} = \rho_c(1 - \tau_w), \quad \rho_{\mathrm{l}}^{\mathrm{sat}} = \rho_c(1 + \tau_w),$$

$$\xi = \sqrt{\frac{\kappa\rho_c^2}{4\tau_w p_c}}, \quad \gamma = \frac{4}{3}\sqrt{2\kappa p_c}(\tau_w)^{3/2}\rho_c. \tag{44}$$

The superscripts in $\rho_{\mathrm{v}}^{\mathrm{sat}}$ and $\rho_{\mathrm{l}}^{\mathrm{sat}}$ mean that these densities are defined under the saturation condition.

There is no universal definition of interface thickness in the literature. In this work, we therefore use ξ as a parameter controlling the interface steepness and define the interfacial region as an the interval of width 10ξ centered at the midpoint density $\rho = \frac{1}{2}(\rho_{\mathrm{v}} + \rho_{\mathrm{l}})$. This convention encompasses the major portion of the diffuse transition layer and is consistent with the visual behavior of the density profiles.

In this work, the value of C_ψ is linked to the interface resolution and we therefore adopt the definition

$$C_\psi = \frac{0.0045}{(\xi/\Delta x)^2}. \tag{45}$$

As the interface resolution is increased (i.e., $\xi/\Delta x$ grows), the value of C_ψ tends to zero, ensuring that the scheme converges

to the original formulation proposed by Wagner under grid refinement. The factor 0.0045 was determined empirically to ensure stability without degrading numerical accuracy. The appropriate value of ξ is obtained through a grid convergence study.

We define the density ratio under the saturation condition as

$$r_\rho^{\mathrm{sat}} = \frac{\rho_\mathrm{l}^{\mathrm{sat}}}{\rho_\mathrm{v}^{\mathrm{sat}}} \Rightarrow r_\rho^{\mathrm{sat}} = \frac{1+\tau_w}{1-\tau_w}. \tag{46}$$

The fluid temperature is directly related to r_ρ^{sat}. Thus, throughout this work, we report r_ρ^{sat} instead of the fluid temperature. Accordingly, the problem is characterized by only three independent dimensionless parameters: $f_\mathrm{p} = p_\mathrm{v}/p_{\mathrm{sat}}$, r_ρ^{sat}, and ν^*.

In this work, the simulations are carried out in a unit system called "lattice units," frequently employed in the LBM literature. In this system, we set $dx = 1$ and $dt = 1$. Also, we fix $\rho_\mathrm{v}^{\mathrm{sat}} = 1$. For each test, we provide the necessary parameters to reproduce our simulations within this unit system. Parameters not explicitly specified can be obtained by matching the dimensionless quantities.

Considering a system of length L^*, we first initialize the density profile using the hyperbolic tangent function,

$$\rho(x^*) = \frac{\rho_\mathrm{v}+\rho_\mathrm{l}}{2} + \frac{\rho_\mathrm{l}-\rho_\mathrm{v}}{2}\tanh\left(\frac{x^* - 0.25L^*}{\sqrt{2}\xi^*}\right), \tag{47}$$

with $\xi^* = \xi\sqrt{p_\mathrm{v}}/(\rho_\mathrm{v}\sqrt{\kappa})$.

The initialization of the velocity profile is discussed later. After defining the macroscopic quantities, the distribution function is initialized to be equal to its equilibrium counterpart (35). Periodic boundary conditions are applied in the bottom and top to reproduce the 1D case. In the side boundaries, the chemical potential and the density are fixed for the vapor value.

A subtle but important numerical aspect concerns the treatment of viscosity in the bulk regions. During the initial transient regime of the simulations, we observed that low-viscosity settings may lead to weak oscillations in the density and velocity fields, which arise from the rapid motion of the interface combined with small residual numerical noise. These oscillations are irrelevant to the physics of the problem, but can slow down the convergence toward the steady interface velocity.

To suppress these transient oscillations efficiently, we adopt a smoothly varying relaxation time $\tau(x)$, assigning the desired relaxation time τ_{int} only in the neighborhood of the interface and using a higher relaxation time $\tau_{\mathrm{bulk}} = 1$ in the bulk region. The transition between the two viscosities is implemented through a hyperbolic-tangent blending function,

$$\phi(x) \;=\; \frac{1}{2}\left[1 - \tanh\left(\frac{|x - x_{\mathrm{int}}| - L_{\mathrm{core}}}{L_{\mathrm{trans}}}\right)\right], \tag{48}$$

where x_{int} is the interface position, L_{core} is the half width of the region where the interface relaxation time is applied (we set $L_{\mathrm{core}} = 12\xi$), and $L_{\mathrm{trans}} = \xi$ controls the thickness of the transition layer. The effective relaxation time is then defined by the convex combination

$$\tau(x) \;=\; \phi(x)\,\tau_{\mathrm{int}} \;+\; [1-\phi(x)]\,\tau_{\mathrm{bulk}}. \tag{49}$$

This smooth transition avoids the spurious reflections that would result from discontinuous viscosity jumps. Importantly, this viscosity modification has *no impact on the final results*. The bulk regions exhibit a uniform velocity, as shown in Fig. 2, implying $\partial_x u = 0$ and therefore a vanishing viscous stress tensor. This fact was confirmed by comparing simulations performed with uniform viscosity and with the spatially varying viscosity described above, which produced indistinguishable interface velocities within numerical precision.

A major difficulty arises at small density ratios. According to the inviscid prediction (28), the interface velocity increases sharply as the density ratio $\rho_\mathrm{l}/\rho_\mathrm{v}$ approaches unity since the denominator of the expression tends to zero in this limit. At the same time, near the critical point, the speed of sound decreases because the equation of state exhibits an inflection point where $dp/d\rho \to 0$. As a result, a regime naturally emerges in which the interface velocity becomes comparable to the acoustic velocity.

For the most critical case investigated in this work ($r_\rho^{\mathrm{sat}} = 2$, $p_\mathrm{v} = 0.96$, p_{sat}, and $\nu^* = 1/64$), we obtain $u_{\mathrm{int}}/u_\mathrm{s} \approx 0.175$, where u_s denotes the isothermal sound speed in the liquid. Although this value remains below the speed of sound, it already places the system in an acoustically stiff regime. In this situation, the time required for pressure waves to propagate from the interface to the domain boundaries and return becomes comparable to the timescale over which the interface itself undergoes a significant displacement, making simulations near the critical point particularly challenging.

For this reason, we introduce a sponge layer in the liquid region to accelerate the dissipation of these pressure waves and thus shorten the transient period. Let $x_{\mathrm{ref}} = x_{\mathrm{int}} + 15\xi$ denote a point in the liquid phase sufficiently close to the interface. The density and chemical potential for $x > x_{\mathrm{ref}}$ are then updated according to

$$\begin{aligned}\rho(x) &\leftarrow (1-\varepsilon)\,\rho(x) \;+\; \varepsilon\,\rho(x_{\mathrm{ref}}),\\ \mu(x) &\leftarrow (1-\varepsilon)\,\mu(x) \;+\; \varepsilon\,\mu(x_{\mathrm{ref}}), \quad x > x_{\mathrm{ref}},\end{aligned} \tag{50}$$

with $\varepsilon = 10^{-3}$, which introduces only a minute relaxation toward $\rho(x_{\mathrm{ref}})$ and $\mu(x_{\mathrm{ref}})$, yet is sufficient to ensure rapid dissipation of the outgoing waves generated during the early interface motion.

Both this boundary sponge and the spatially varying relaxation time serve exclusively to suppress the early-time transients. Once the interface velocity approaches its asymptotic regime, these numerical aids are switched off and the simulation proceeds with uniform viscosity and without any damping.

Next, we assess the influence of these stabilization strategies. We begin by considering three cases without any numerical aid, shown in the top panel of Fig. 4. For this comparison, we use the vapor velocity at the left boundary of the system. This choice is motivated by the difficulty of tracking the interface velocity in the transient regime since strong acoustic waves can affect the density profile in the interfacial region without representing an actual advection of the interface.

In case 1, the system is initialized using the analytical velocity profile from Eqs. (33)–(10). In case 2, the velocity field is initialized to zero. Case 3 is also initialized with zero

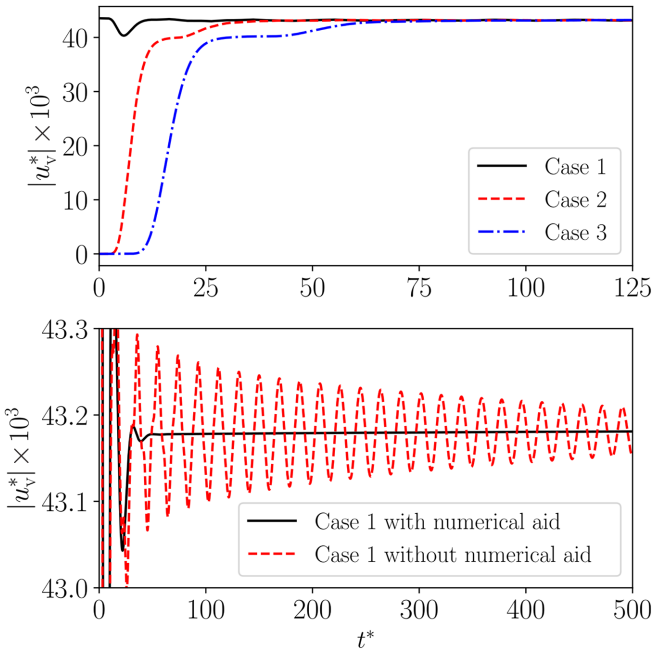

FIG. 4. Vapor phase velocity magnitude $|u_v^*|$ at left boundary over time t^* for LBM simulations in openlb [43]. All cases use $r_\rho^{sat} = 32$, $p_v = 0.95 p_{sat}$, and $\nu^* = 1.0$. Top: Case 1 ($L^* = 50$), initialized with the analytical velocity profile. Case 2 ($L^* = 50$), initialized with zero velocity. Case 3 ($L^* = 100$), initialized with zero velocity. Bottom: Comparison between Case 1 without numerical aid and a corresponding simulation employing both stabilization strategies (49) and (50). We set $\gamma = 1.5/\epsilon$ in lattice units.

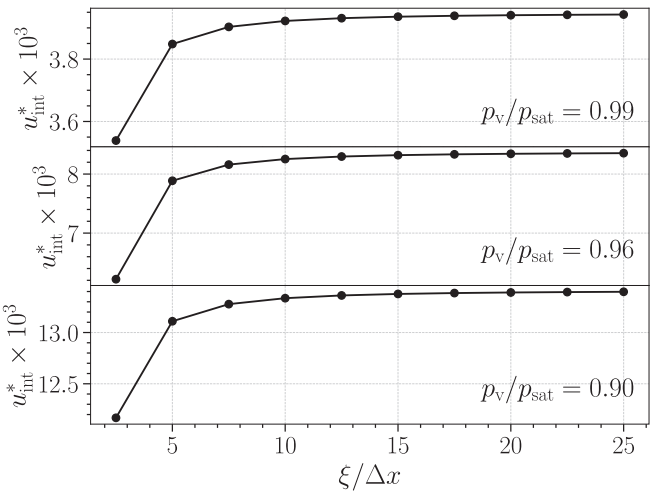

FIG. 5. Interface velocity u_{int}^* dependency on interface resolution $\xi/\Delta x$ for LBM simulations in openlb [43]. Results using $\nu^* = 1/64$ and setting $\gamma = 1.5/\epsilon$ in lattice units.

velocity, but employs a longer computational domain. Although the transient period differs between the three cases, all of them converge to the same steady vapor velocity, regardless of the initial condition or domain length. Therefore, we adopt the analytical initialization to reduce the transient duration.

In the bottom panel of Fig. 4, we examine the combined effect of the sponge layer and the increased bulk viscosity. We compare case 1 without any aid to an otherwise identical simulation where both stabilization strategies are applied. Both simulations converge to the same interface velocity (since the relaxation time at the interface is the same), but the simulation with numerical aid converges substantially faster, as the oscillations produced during initialization decay much more rapidly.

Although none of the numerical aids introduced above were found to affect the final steady-state interface velocity, we nevertheless disable all stabilization mechanisms as soon as the interface reaches its terminal velocity in every simulation. This ensures that the reported results are entirely free from any influence of the numerical tools used solely to shorten the transient period.

Finally, before presenting the results, we conducted a mesh study to determine the appropriate resolution for the simulations. To this end, we ran three cases with $r_\rho^{sat} = 32$, $\nu^* = 1/64$ considering pressure fractions $f_p = 0.99$, 0.96, and 0.90. Since domain length is not relevant, we used the interface resolution, given by $\xi/\Delta x$, as a measure of simulation resolution. This value provides an estimate of the number of nodes that occupy the interface. We set $\gamma = 1.5/\xi$ in lattice units; this choice keeps κ constant for all grids.

The results are presented in Fig. 5. The difference in u_{int} between resolutions 15 and 25 was smaller than 0.5% for $f_p = 0.90$ and 0.96. For $f_p = 0.99$, larger grids were necessary to achieve this variation. Thus, for this specific case ($r_\rho^{sat} = 32$ and $f_p = 0.99$), we divide our C_ψ by a factor of 10 to increase the precision at lower resolutions. Figure 5 already incorporates this change. With this modification, the differences between resolutions 15 and 25 were smaller than 0.18%. The same test was repeated for $r_\rho^{sat} = 8$ and $r_\rho^{sat} = 2$. We concluded that for all cases, $\xi/\Delta x = 15$ was enough while using C_ψ of (45). The only exception in this work is the case $r_\rho^{sat} = 32$ with $f_p = 0.99$, for which C_ψ is divided by a factor of 10 to maintain $\xi/\Delta x = 15$.

VI. RESULTS

A. Verification of the modeling framework

Before testing the inviscid analytical solution (28) and the approximate viscous solution (33), we first validate the physical equations underlying our approach. The validation is based on comparisons with numerical simulations using the free-energy LBM proposed by Wagner [47] and implemented in openlb [43]. The results demonstrate that the observed effects arise directly from the governing physical equations.

Equation (16) is crucial to our work, as it describes the pressure variations given by (4) resulting from momentum exchange and viscous forces acting at the interface. To assess the contribution of each term, we adopt the following definitions:

$$p_{nonideal} \coloneqq p_{EOS} + \frac{\kappa}{2}\left(\frac{\partial \rho}{\partial x'}\right)^2 - \kappa\rho\frac{\partial^2 \rho}{\partial x'^2}, \tag{51a}$$

$$p_{momentum} \coloneqq p_v + \rho_l^2 u_{int}^2\left(\frac{1}{\rho_v} - \frac{1}{\rho}\right), \tag{51b}$$

$$p_{friction} \coloneqq p_v + 2\rho_l u_{int}\rho\frac{d\rho}{dx'}, \tag{51c}$$

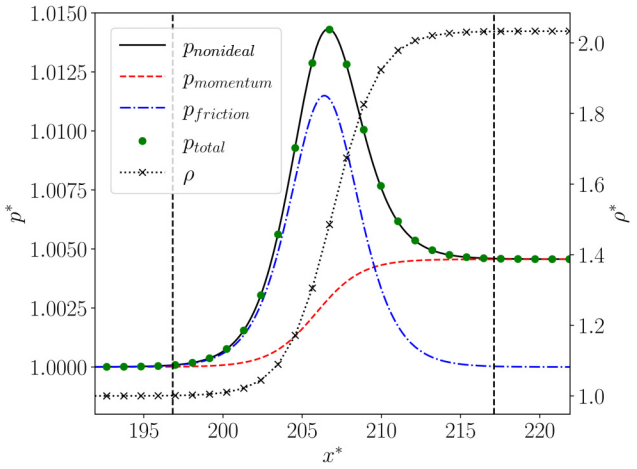

FIG. 6. Pressure p^* (left vertical axis) and density ρ^* (right vertical axis) along domain length x^*. Dimensionless quantities are defined in (5). Pressure definitions are given in (51). Simulation results with $r_\rho^{\text{sat}} = 2$, $p_{\text{v}} = 0.99 p_{\text{sat}}$, and $\nu^* = 0.5$ obtained from LBM implemented in openlb [43]. The vertical lines represent the boundaries of the diffuse interface according to the convention defined in Sec. V. We set $\gamma = 10^{-4}$ in lattice units.

$$p_{\text{total}} := p_{\text{v}} + \rho_{\text{l}}^2 u_{\text{int}}^2 \left(\frac{1}{\rho_{\text{v}}} - \frac{1}{\rho} \right) + 2\rho_{\text{l}} u_{\text{int}} \frac{\nu}{\rho} \frac{d\rho}{dx'}. \quad \text{(51d)}$$

We perform an LBM simulation with $r_\rho^{\text{sat}} = 2$, $p_{\text{v}} = 0.99 p_{\text{sat}}$, and $\nu^* = 0.5$, and run the simulation until a steady-state velocity solution is reached. From the resulting density and velocity fields, we compute (51a)–(51d). The first- and second-order derivatives in these equations are approximated using central finite differences with second-order accuracy.

Figure 6 shows the density profile for this simulation and the variation of p_{nonideal} and p_{total} across the interfacial region. Both pressures are equivalent, which is consistent with (16). We observe that when moving from the vapor region across the interface, p_{nonideal} increases, reaching a peak inside the interfacial region, and then decreases toward the liquid region. The value of p_{nonideal} is higher in the liquid region than in the vapor region.

In Fig. 6, we observe that p_{momentum} grows continuously from the vapor region to the liquid region due to momentum exchange across the interface. In the bulk regions, p_{nonideal} equals p_{momentum}, indicating that momentum exchange is solely responsible for the pressure difference between bulk phases.

Finally, we also plot p_{friction} in Fig. 6. The value of this quantity grows inside the interface due to the velocity gradient across the interface. However, friction does not contribute to the pressure difference between the two bulk phases. The numerical results are fully consistent with the proposed physical model.

B. Comparison with lattice Boltzmann method

We compare the analytical approximation given by (33) against results obtained from LBM simulations. To assess the robustness of the model, we consider three representative density ratios, $r_\rho^{\text{sat}} = 2$, 8, and 32. We then analyze how the interface velocity u_{int}^* varies as a function of the kinematic viscosity ν^*. Simulations are performed across a range of pressure ratios defined as $f_{\text{p}} = p_{\text{v}}/p_{\text{sat}}$.

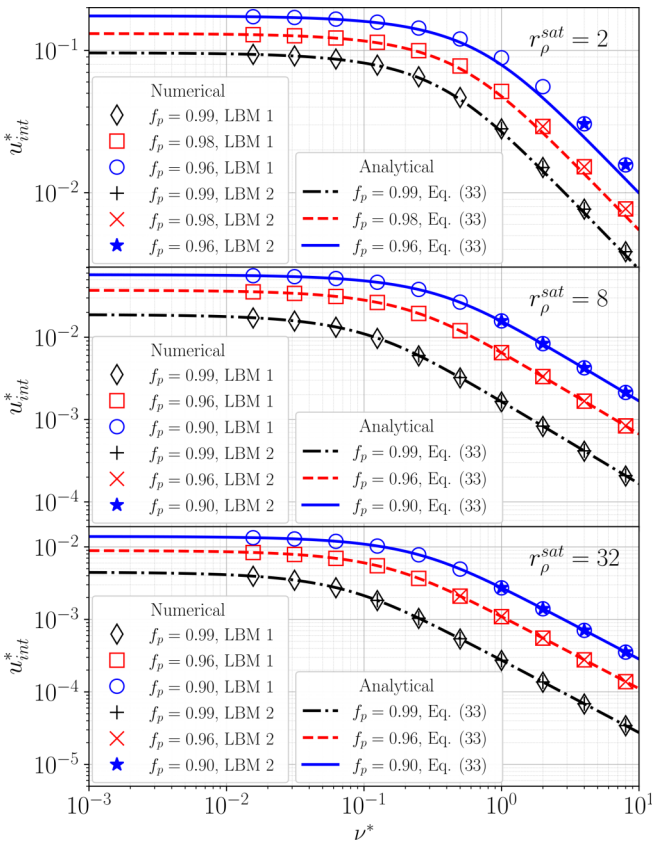

FIG. 7. Dependency of interface velocity u_{int}^* on fluid kinematic viscosity ν^* for fixed r_ρ^{sat} and different values of $f_{\text{p}} = p_{\text{v}}/p_{\text{sat}}$. Dimensionless quantities are defined in (5). Points represent simulation results using LBM implemented in openlb [43]. LMB 1 is respective to simulations using C_ρ value as (45) (with exception of $r_\rho^{\text{sat}} = 32$ and $f_{\text{p}} = 0.99$ where we divide C_ρ by 10) and LBM 2 to $C_\rho = 0$.

In all simulations, the interface is initially positioned at $x = 0.25L$, where L denotes the length of the computational domain. The simulations are then carried out until the interface reaches $x = 0.75L$. To accelerate the transient evolution and reduce the computational cost, auxiliary numerical techniques are employed during the early stages of the simulation (49) and (50). These numerical aids are completely switched off once the interface reaches the midpoint of the domain, $x = 0.5L$, ensuring that all measurements of the interface velocity are performed under unbiased dynamical conditions. In addition, these numerical aids are applied only in simulations with $\nu^* < 1$. The simulations with $r_\rho^{\text{sat}} = 2$, 8, and 32 employ $\gamma = 10^{-4}$, 5×10^{-3}, and 0.1, respectively, in lattice units.

Two distinct sets of simulations are performed, denoted as LBM 1 and LBM 2. In LBM 1, the stabilization parameter C_ψ is set according to (45) in order to enhance numerical stability, whereas in LBM 2 we strictly enforce $C_\psi = 0$. As shown in Fig. 7, the use of a nonzero C_ψ significantly enlarges the range of stable simulations, enabling cases that could not be simulated otherwise. Importantly, the comparison between LBM 1 and LBM 2 demonstrates that the introduction of this

TABLE I. Relative error between the analytical approximation and LBM simulations for different density ratios r_ρ^{sat}, pressure fractions f_p, and viscosities ν^*.

r_ρ^{sat}	f_p	ν^*	Relative error (%)
32	0.99	1/64	0.27
32	0.99	8	0.50
32	0.90	1/64	0.24
32	0.90	8	0.24
8	0.99	1/64	0.64
8	0.99	6.4	1.04
8	0.90	1/64	0.05
8	0.90	8	1.51
2	0.99	1/64	0.02
2	0.99	8	6.27
2	0.96	1/64	0.04
2	0.96	8	26.36

numerical stabilization does not affect the physical results: Both approaches yield indistinguishable interface velocities within numerical accuracy. This confirms that the proposed stabilization strategy improves robustness without altering the underlying dynamics.

It is important to note that the viscid solution given by (33) is an approximation and may deviate from the exact solution of the underlying differential equation. However, the free-energy LBM is a consistent numerical method for solving the mass and momentum conservation equations, and its results converge to the exact solution as the spatial and temporal resolution increases. Therefore, we use high-resolution LBM simulations as a reference to assess the accuracy of our analytical approximation.

The results of this comparison are shown in Fig. 7. The overall behavior of the solution is qualitatively similar across all cases. For very low viscosities, the solution converges to the inviscid limit given by (28). Conversely, when ν^* is sufficiently large, the interface velocity becomes small and the quadratic term u_{int}^2 in (32a) can be neglected. In this high-viscosity regime, the interface velocity exhibits an inverse dependence on the viscosity.

The difference observed between the numerical and analytical solutions arises from using the inviscid solution $z^{(0)}$ as an approximation for the actual solution z in (31). As the results show that the interface velocity u_{int} decreases significantly with increasing density ratio, the product νu_{int} in (21) remains small, making the viscous effect less relevant. Consequently, the inviscid solution $z^{(0)}$ becomes closer to the actual one and the approximation based on the inviscid case becomes more accurate for high density ratios.

A selection of relative errors between the analytical approximation and the LBM results is compiled in Table I. Three main trends can be identified from the data: First, the approximation becomes less accurate as the viscosity ν^* increases. This is consistent with the construction of our solution, which is derived from the inviscid limit and, therefore, performs best in low-viscosity regimes. Second, the error also increases as the pressure fraction $f_\text{p} = p_\text{v}/p_{\text{sat}}$ decreases. A third trend is observed with respect to the density ratio. For lower values such as $r_\rho^{\text{sat}} = 2$, the approximation becomes significantly less accurate.

This suggests that near the critical point—where the density ratio approaches unity—the interface becomes more sensitive to viscous effects. Since our approximation relies on the assumption of proximity to the inviscid case, its accuracy degrades in this regime, where the influence of viscosity becomes more pronounced.

These observations help delineate the validity range of the proposed approximation. The solution consistently yields accurate results in the low-viscosity regime. Moreover, we observe that if the density ratio remains above 8 and the pressure fraction exceeds 0.90, the approximation remains reliable across a broad range of viscosities. For $r_\rho^{\text{sat}} = 2$, however, the pressure fraction should be kept below 0.99 in order to get accurate results.

C. Comparison with sharp-interface solution

Jamet [45] modeled a similar problem using a sharp-interface approach. His formulation is based on the framework originally proposed by Ishii [66], which is derived from applying jump conditions across the interface under the assumption of thermodynamic equilibrium. Under this assumption, the following equation is obtained (see Ishii [66, p. 41, Eqs. (2)–(106)] and Jamet [45, Eq. (16)]):

$$p_\text{v} = p_{\text{sat}} - \frac{1}{2}\frac{\rho_v \rho_l}{\rho_l - \rho_v}(u_v - u_l)^2. \tag{52}$$

Assuming symmetry in our test case, such that $u_\text{l} = 0$, and using (10), we obtain

$$u_{\text{int}} = \sqrt{\frac{p_{\text{sat}} - p_\text{v}}{\frac{\rho_\text{l}^2}{2}\left(\frac{1}{\rho_\text{v}} - \frac{1}{\rho_\text{l}}\right)}}. \tag{53}$$

This relation shares similarities with (28). In fact, (53) can be derived from (28) if we assume

$$\int_{\rho_v}^{\rho_l} \frac{p_{\text{EOS}}}{\rho^2}\, d\rho \approx \int_{\rho_v}^{\rho_l} \frac{p_{\text{sat}}}{\rho^2}\, d\rho. \tag{54}$$

This is essentially the Maxwell construction, which holds under thermodynamic equilibrium. However, under nonequilibrium conditions, this approximation may no longer be valid. Moreover, this macroscopic model does not capture the dependence of the evaporation flux on viscosity.

Next, we compare our inviscid solution (28) with the sharp-interface model given by (53). The results for different values of r_ρ^{sat} and f_p are shown in Fig. 8. Overall, the two solutions exhibit excellent agreement. Noticeable deviations are observed only when f_p is significantly reduced (e.g., to 0.7) or near the critical point, where r_ρ^{sat} approaches unity.

The small discrepancies observed in Fig. 8 originate from the approximation in (54), which replaces the integral of p_{EOS} by its equilibrium Maxwell construction. This approximation is exact only under thermodynamic equilibrium, whereas our diffuse-interface solution is obtained for a nonequilibrium evaporation process with finite mass flux and a pressure below saturation. As a result, the sharp-interface model assumes an interface that instantaneously satisfies equilibrium conditions, while the diffuse model captures deviations from equilibrium

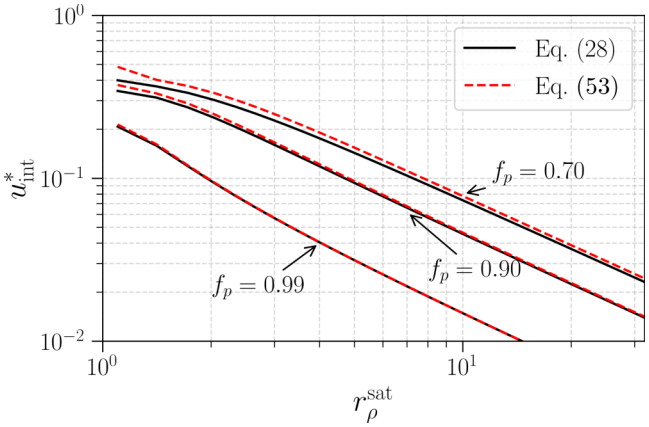

FIG. 8. Dependency of interface velocity $u^*_{\rm int}$ on the density ratio $r^{\rm sat}_\rho$ for different values of $f_{\rm p} = p_{\rm v}/p_{\rm sat}$. Plot shows a comparison between our inviscid solution (28) and Jamet solution (53).

across the transition layer. These deviations become more pronounced as the density ratio approaches unity or as $p_{\rm v}/p_{\rm sat}$ decreases, explaining the increasing difference between the two predictions.

For general purposes, we conclude that the two models yield comparable predictions across a wide range of conditions. In future work, we intend to extend this comparison by incorporating LBM simulations using more stable collision operators. At present, the use of the single-relaxation-time operator restricts our ability to access sufficiently low viscosities to fully explore the inviscid regime.

VII. CONCLUSION

This work presents an analytical approximation to the problem of isothermal evaporation under subsaturation pressure conditions using a diffuse-interface model. For the inviscid case, our solution is exact. By avoiding traditional assumptions such as local thermodynamic equilibrium at the interface, the proposed approach offers a different perspective on the relationship between evaporation rates and viscosity. The derived solution is evidenced against numerical simulation results produced with an LBM implemented in openlb, demonstrating excellent agreement and reinforcing its physical consistency.

The findings highlight the potential of diffuse-interface models in studying phase-change phenomena, not only as a predictive tool but also as a benchmark for numerical methods. The results provide clear evidence that the evaporation dynamics, including interface velocity, are strongly influenced by fluid viscosity, which is often overlooked in the existing literature. Furthermore, this found analytical solution can serve as a reference for experimental validation of diffuse interface methodologies or as a basis for future refinements of these models.

Future work could extend this approach to nonisothermal conditions and multicomponent systems, enabling broader applications in practical scenarios such as fuel atomization and heat-transfer processes. By bridging the gap between analytical models and numerical simulations, this study contributes to a more comprehensive and accurate modeling of phase-change phenomena in complex systems.

The simulation code used to generate all numerical results shown in the manuscript is available in Ref. [63].

ACKNOWLEDGMENT

We acknowledge the support of the Alexander von Humboldt Foundation (AvH) through a Humboldt Research Fellowship awarded to L.E.C. at LBRG, KIT.

DATA AVAILABILITY

The data that support the findings of this article are not publicly available. The data are available from the authors upon reasonable request.

[1] F. Fathi, S. N. Ebrahimi, L. C. Matos, M. B. P. P. Oliveira, and R. C. Alves, Emerging drying techniques for food safety and quality: A review, Compr. Rev. Food Sci. Food Saf. **21**, 1125 (2022).

[2] A. S. I. Al-Jammali, A. A. Amooey, and S. R. Nabavi, Multi-objective particle swarm optimization of industrial natural gas dehydration process, Chemical Papers **77**, 1067 (2023).

[3] M. Skiborowski, Synthesis and design methods for energy-efficient distillation processes, Curr. Opin. Chem. Eng. **42**, 100985 (2023).

[4] A. M. Abdelrahman, A. Khadir, D. Santoro, E. Jang, A. Al-Omari, C. Muller, K. Y. Bell, J. Walton, D. Batstone, and G. Nakhla, Vacuum evaporation coupled with anaerobic digestion for process intensification and ammonia recovery: Model development, validation and scenario analysis, Bioresour. Technol. **416**, 131753 (2025).

[5] V. Di Tullio, R. Pigliapochi, N. Zumbulyadis, S. A. Centeno, J. Catalano, M. Wagner, and C. Dybowski, Dynamics of diffusion, evaporation, and retention of organic solvents in paints by unilateral NMR and HR-MAS NMR spectroscopy, Microchem. J. **190**, 108582 (2023).

[6] S. Abdullah, M. N. B. M. Zubir, M. R. B. Muhamad, K. M. S. Newaz, H. F. Öztop, M. S. Alam, and K. Shaikh, Technological development of evaporative cooling systems and its integration with air dehumidification processes: A review, Energy Build. **283**, 112805 (2023).

[7] C. Polski, T. Polski, J. Roman, R. Wróblewski, J. Bartoszewicz, and B. Ceran, A novel concept to improve the flexibility of steam power plants using an electric feedwater heater, Appl. Therm. Eng. **236**, 121661 (2024).

[8] H. Hertz, On the evaporation of liquids, especially mercury, in a vacuum, Ann. Phys. **253**, 177 (1882).

[9] M. Knudsen, The molecular flow of gases through openings and effusion, Ann. Phys. **333**, 999 (1909).

[10] R. Hołyst, M. Litniewski, and D. Jakubczyk, A molecular dynamics test of the Hertz-Knudsen equation for evaporating liquids, Soft Matter **11**, 7201 (2015).

[11] A. H. Persad and C. A. Ward, Expressions for the evaporation and condensation coefficients in the Hertz-Knudsen relation, Chem. Rev. **116**, 7727 (2016).
[12] R. W. Schrage, *A Theoretical Study of Interphase Mass Transfer* (Columbia University Press, New York, 1953).
[13] J. Stefan, On the theory of ice formation, in particular on ice formation in the polar seas, Ann. Phys. **278**, 269 (1891).
[14] L. Scriven, On the dynamics of phase growth, Chem. Eng. Sci. **50**, 3907 (1995).
[15] G. E. Cossali and S. Tonini, Analytical solutions for modelling the evaporation of sessile drops, Appl. Math. Modell. **114**, 61 (2023).
[16] J. C. Álvarez-Hostos, M. R. Mascotto, A. D. Bencomo, A. J. Sarache-Piña, and V. D. Fachinotti, A fully analytical solution for 1D advection-conduction heat transfer problems with non-isothermal solid ↔ liquid phase change, Intl. Commun. Heat Mass Transfer **153**, 107327 (2024).
[17] F. Municchi, I. El Mellas, O. Matar, and M. Magnini, Conjugate heat transfer effects on flow boiling in microchannels, Intl. J. Heat Mass Transf. **195**, 123166 (2022).
[18] J. Wang, G. Liang, X. Yin, and S. Shen, Pool boiling on micro-structured surface with lattice Boltzmann method, Intl. J. Therm. Sci. **187**, 108170 (2023).
[19] F. Municchi, C. Markides, O. Matar, and M. Magnini, Computational study of bubble, thin-film dynamics and heat transfer during flow boiling in noncircular microchannels, Appl. Therm. Eng. **238**, 122039 (2024).
[20] S. Manova, L. G. Asirvatham, A. A. Appadurai, G. Ribatski, P. Kumar, and S. Wongwises, An experimental investigation on the heat transfer characteristics of minichannel thermosyphon with multiports for cooling the modern miniaturized electronic devices, Energy Convers. Manage. **268**, 115997 (2022).
[21] V. E. C. Baptistella, T. A. Moreira, and G. Ribatski, Liquid-film thickness during flow boiling of pure hydrocarbons and their mixtures, Expt. Therm. Fluid Sci. **144**, 110877 (2023).
[22] D. B. Marchetto, R. Revellin, R. Rullière, and G. Ribatski, An experimental investigation on R245fa and R1233zd(E) flow boiling at high saturation temperatures in a horizontal small diameter channel, Intl. J. Heat Mass Transf. **220**, 124986 (2024).
[23] D. Jacqmin, Calculation of Two-Phase Navier-Stokes Flows Using Phase-Field Modeling, J. Comput. Phys. **155**, 96 (1999).
[24] A. G. Lamorgese, D. Molin, and R. Mauri, Phase Field Approach to Multiphase Flow Modeling, Milan J. Math. **79**, 597 (2011).
[25] J. Kim, Phase-field models for multi-component fluid flows, Commun. Comput. Phys. **12**, 613 (2012).
[26] A. Novick-Cohen, in *Handbook of Differential Equations: Evolutionary Equations*, edited by C. M. Dafermos and M. Pokorný (Elsevier B.V., 2008), Vol. 4, p. 201.
[27] D. Lee, J.-Y. Huh, D. Jeong, J. Shin, A. Yun, and J. Kim, Physical, mathematical, and numerical derivations of the Cahn-Hilliard equation, Comput. Mater. Sci. **81**, 216 (2014).
[28] X. Feng and A. Prohl, Numerical analysis of the Allen-Cahn equation and approximation for mean curvature flows, Numer. Math. **94**, 33 (2003).
[29] H. L. Wang, Z. H. Chai, B. C. Shi, and H. Liang, Comparative study of the lattice Boltzmann models for Allen-Cahn and Cahn-Hilliard equations, Phys. Rev. E **94**, 033304 (2016).
[30] X. Feng, Y. He, and C. Liu, Analysis of finite element approximations of a phase field model for two-phase fluids, Math. Comput. **76**, 539 (2007).
[31] L. Qiao, Z. Zeng, and H. Xie, Phase-field-based finite volume method for simulating thermocapillary flows, Proc. Eng. **126**, 507 (2015).
[32] H. Hua, J. Shin, and J. Kim, Level set, phase-field, and immersed boundary methods for two-phase fluid flows, J. Fluids Eng. **136**, 021301 (2014).
[33] M. R. Swift, E. Orlandini, W. R. Osborn, and J. M. Yeomans, Lattice Boltzmann simulations of liquid-gas and binary fluid systems, Phys. Rev. E **54**, 5041 (1996).
[34] C. Semprebon, T. Krüger, and H. Kusumaatmaja, Ternary free-energy lattice Boltzmann model with tunable surface tensions and contact angles, Phys. Rev. E **93**, 033305 (2016).
[35] S. Simonis, J. Nguyen, S. J. Avis, W. Dörfler, and M. J. Krause, Binary fluid flow simulations with free energy lattice Boltzmann methods, Discrete Contin. Dyn. Syst. S **17**, 3278 (2024).
[36] X. Shan and H. Chen, Lattice Boltzmann model for simulating flows with multiple phases and components, Phys. Rev. E **47**, 1815 (1993).
[37] X. Shan and H. Chen, Simulation of nonideal gases and liquid-gas phase transitions by the lattice Boltzmann equation, Phys. Rev. E **49**, 2941 (1994).
[38] S. Ito, J. Jeßberger, S. Simonis, F. Bukreev, A. Kummerländer, A. Zimmermann, G. Thäter, G. R. Pesch, J. Thöming, and M. J. Krause, Identification of reaction rate parameters from uncertain spatially distributed concentration data using gradient-based PDE constrained optimization, Comput. Math. Applic. **167**, 249 (2024).
[39] F. Bukreev, S. Simonis, A. Kummerländer, J. Jeßberger, and M. J. Krause, Consistent lattice Boltzmann methods for the volume averaged Navier-Stokes equations, J. Comput. Phys. **490**, 112301 (2023).
[40] F. Bukreev, A. Kummerländer, J. Jeßberger, D. Teutscher, S. Simonis, D. Bothe, and M. J. Krause, Benchmark simulation of laminar reactive micromixing using lattice Boltzmann methods, AIAA J. **63**, 1295 (2025).
[41] A. Mink, K. Schediwy, C. Posten, H. Nirschl, S. Simonis, and M. J. Krause, Comprehensive computational model for coupled fluid flow, mass transfer, and light supply in tubular photobioreactors equipped with glass sponges, Energies **15**, 7671 (2022).
[42] A. Kummerländer, F. Bukreev, S. F. R. Berg, M. Dorn, and M. J. Krause, in *High Performance Computing in Science and Engineering '22*, edited by W. E. Nagel, D. H. Kröner, and M. M. Resch (Springer Nature, Cham, 2024), pp. 233–247,
[43] M. J. Krause, A. Kummerländer, S. J. Avis, H. Kusumaatmaja, D. Dapelo, F. Klemens, M. Gaedtke, N. Hafen, A. Mink, R. Trunk, J. E. Marquardt, M.-L. Maier, M. Haussmann, and S. Simonis, OpenLB—Open source lattice Boltzmann code, Comput. Math. Appl. **81**, 258 (2020).
[44] E. M. Foard and A. J. Wagner, Enslaved phase-separation fronts in one-dimensional binary mixtures, Phys. Rev. E **79**, 056710 (2009).
[45] D. Jamet, Test-case no 7B: Isothermal vaporization due to piston aspiration (pa), Multiphase Sci. Technol. **16**, 61 (2004).
[46] W. Zeng, M. Xu, G. Zhang, Y. Zhang, and D. J. Cleary, Atomization and vaporization for flash-boiling multi-hole sprays with alcohol fuels, Fuel **95**, 287 (2012).

[47] A. J. Wagner, Thermodynamic consistency of liquid-gas lattice Boltzmann simulations, Phys. Rev. E **74**, 056703 (2006).

[48] T. Krüger, H. Kusumaatmaja, A. Kuzmin, O. Shardt, G. Silva, and E. M. Viggen, *The Lattice Boltzmann Method: Principles and Practice* (Springer, Cham, 2017), p. 4.

[49] W. G. Vincenti, C. H. Kruger, Jr., and T. Teichmann, Introduction to physical gas dynamics, Phys. Today **19**(10), 95 (1966).

[50] G. G. Stokes, On the theories of the internal friction of fluids in motion, and of the equilibrium and motion of elastic solids, Trans. Cambridge Philos. Soc. **8**, 287 (1845).

[51] R. E. Graves and B. M. Argrow, Bulk viscosity: Past to present, J. Thermophys. Heat Transfer **13**, 337 (1999).

[52] S. Kosuge and K. Aoki, Navier–stokes equations and bulk viscosity for a polyatomic gas with temperature-dependent specific heats, Fluids **8**, 5 (2022).

[53] P. L. Bhatnagar, E. P. Gross, and M. Krook, A model for collision processes in gases. I. Small amplitude processes in charged and neutral one-component systems, Phys. Rev. **94**, 511 (1954).

[54] D. J. Korteweg, On the form of the equations of motion of fluids when capillary forces due to density variations are taken into account, Arch. Néerl. Sci. Exactes Nat. **6**, 1 (1901).

[55] L. Bougoffa, New exact general solutions of Abel equation of the second kind, Appl. Math. Comput. **216**, 689 (2010).

[56] F. Bukreev, F. Raichle, H. Nirschl, and M. J. Krause, Simulation of adsorption processes on moving particles based on an Euler-Euler description using a lattice Boltzmann discretization, Chem. Eng. Sci. **270**, 118485 (2023).

[57] N. Hafen, J. E. Marquardt, A. Dittler, and M. J. Krause, Simulation of particulate matter structure detachment from surfaces of wall-flow filters for elevated velocities applying lattice Boltzmann methods, Fluids **8**, 99 (2023).

[58] J. E. Marquardt, N. Hafen, and M. J. Krause, A novel particle decomposition scheme to improve parallel performance of fully resolved particulate flow simulations, J. Comput. Sci. **78**, 102263 (2024).

[59] M. Siodlaczek, M. Gaedtke, S. Simonis, M. Schweiker, N. Homma, and M. J. Krause, Numerical evaluation of thermal comfort using a large eddy lattice Boltzmann method, Build. Environ. **192**, 107618 (2021).

[60] S. Simonis, D. Oberle, M. Gaedtke, P. Jenny, and M. J. Krause, Temporal large eddy simulation with lattice Boltzmann methods, J. Comput. Phys. **454**, 110991 (2022).

[61] F. Reinke, N. Hafen, M. Haussmann, M. Novosel, M. J. Krause, and A. Dittler, Applied geometry optimization of an innovative 3D-printed wet-scrubber nozzle with a lattice Boltzmann method, Chem. Ing. Tech. **94**, 348 (2022).

[62] J. Jeßberger, J. E. Marquardt, L. Heim, J. Mangold, F. Bukreev, and M. J. Krause, Optimization of a micromixer with automatic differentiation, Fluids **7**, 144 (2022).

[63] A. Kummerländer, T. Bingert, F. Bukreev, L. E. Czelusniak, D. Dapelo, C. Gaul, N. Hafen, S. Ito, J. Jeßberger, D. Khazaeipoul, T. Krüger, H. Kusumaatmaja, J. E. Marquardt, A. Raeli, M. Rennick, F. Prinz, M. Schecher, A. Schneider, Y. Shimojima, *et al.*, openlb release 1.8: Open source lattice Boltzmann code (1.8.0), https://www.openlb.net/download/ (2025).

[64] Q. Li, K. H. Luo, and X. J. Li, Forcing scheme in pseudopotential lattice Boltzmann model for multiphase flows, Phys. Rev. E **86**, 016709 (2012).

[65] A. J. Briant, A. J. Wagner, and J. M. Yeomans, Lattice Boltzmann simulations of contact line motion. I. Liquid-gas systems, Phys. Rev. E **69**, 031602 (2004).

[66] M. Ishii, Thermo-fluid dynamic theory of two-phase flow, NASA Technical Report No. NASA-STI/Recon-75-29657 (Eyrolles, Paris, 1975).